Elastic properties of ultrathin permalloy/alumina multilayer films using picosecond ultrasonics and Brillouin light scattering

Clément Rossignol,* Bernard Perrin, and Bernard Bonello
Laboratoire des Milieux Désordonnés et Hétérogènes, UMR CNRS 7603, Université Pierre et Marie Curie, 4 Place Jussieu, 75252 Paris Cedex 05, France

Philippe Djemia and Philippe Moch
Laboratoire des Propriétés Mécaniques et Thermodynamiques des Matériaux, UPR CNRS 9001, Université Paris-Nord, 99 av. J.B. Clément, 93430 Villetaneuse Cedex, France

Hervé Hurdequint
Laboratoire de Physique des Solides, UMR CNRS 8502, Université Paris-Sud, 91405 Orsay Cedex, France
(Received 17 September 2003; revised manuscript received 11 February 2004; published 3 September 2004)

Picosecond ultrasonics and Brillouin light scattering were used to investigate the acoustical properties of periodic (Py-Al_2O_3) multilayers constituted of ultrathin polycrystalline layers of permalloy (Py corresponding to a $Ni_{80}Fe_{20}$ alloy) separated by a dielectric spacer of amorphous alumina (Al_2O_3). Picosecond ultrasonics gives access to the elastic properties of multilayers both through the travel time of acoustic echoes propagating in the whole structure and through the frequencies of localized vibrational modes lying within the gaps induced by the periodicity of the system. These measurements show that the effective longitudinal elastic constant along the bilayer stacking axis, softens from 7% to 40%, with respect to a reference value obtained in thick samples, when the period decreases from 14.8 to 5.3 nm. This strong softening is ascribed to interfacial effects between permalloy and alumina layers. In contrast with the longitudinal elastic constant, the softening of the in-plane shear elastic constant, derived from Brillouin light scattering measurements, does not exceed 10% for the smallest period sample.

DOI: 10.1103/PhysRevB.70.094102 PACS number(s): 78.47.+p, 78.35.+c, 62.20.Dc, 68.60.Bs

I. INTRODUCTION

In recent years, nanometer-scaled multilayers and superlattices received increasing interest owing to the observation of novel and unexpected structural and mechanical properties in these systems.[1] For example, results obtained from Brillouin light scattering experiments evidenced the softening of the shear elastic constant with decreasing bilayer period in metallic superlattices made of nonmiscible constituents corresponding to either bcc-fcc, bcc-bcc or fcc-fcc structures, such as Cr-Au, Nb-Cu, Mo-Ni, Ni-V, Mo-Ta, Ag-Ni, Co-Cu.[2–8] Picosecond ultrasonics experiments gave also evidence of the softening of the longitudinal elastic constant with decreasing bilayer thickness in Cu-W, Ni-Mo, Ni-Pt, Ni-Ti, and Fe-Cu multilayers.[9–11] Softening with respect to the expected values deduced from the bulk material properties (or obtained for large periods as reference values) of both shear and longitudinal elastic constants up to 25%–30% have been observed. These elastic anomalies have generally been ascribed to interfacial effects: interfacial strain originating from interfacial expansion or interfacial extended disorder.[10–12] The picosecond ultrasonics technique has been also used to characterize the elasticity of a layered structure with a broad interface, a diffuse interface or a modified interfacial bonding resulting from ion implantation.[13–16] Most studies of interfacial effects have dealt with metallic materials and only very few reports are relative to metal-insulator composite systems.[17,18] One may note also that the first metal-insulator system investigated[18] (NbN-AlN superlattices), showing no elastic anomaly with decreasing bilayer period, corresponded to a multilayered structure where both constituents are crystalline. By contrast, in the present study, we are dealing with a magnetic composite system (permalloy-alumina) where the ultrathin layers of these two materials are, respectively, polycrystalline and amorphous. Such magnetic metal-dielectric multilayers are of great interest for a large range of applications such as high-density storage media, spintronics, etc. It appears thus important to investigate in detail their mechanical properties.

In this work, the picosecond ultrasonics and the Brillouin light scattering techniques are associated to study thick single layers, respectively, of permalloy (Py: $Ni_{80}Fe_{20}$) and of amorphous alumina (Al_2O_3) as well as a whole series of (Py-Al_2O_3) multilayers corresponding to a periodic stacking of ultrathin layers of these constituents. Our goal was to determine the elastic parameters of these multilayers corresponding to a composite system known to form sharp interfaces (see, for example, Fe-Al_2O_3 superlattices)[19] and to study their dependence on interfacial effects. Picosecond ultrasonics measurements and Brillouin light scattering spectra are described and compared to numerical simulations resulting from analytical models respectively for the reflectivity changes and for the spectral density related to the phonon normal displacement amplitude at the free surface. The elastic constants of permalloy and of alumina single layers measured by the two methods are compared and used to describe the elastic behavior of the multilayers.

TABLE I. Main characteristics of the series of $[\text{Py-Al}_2\text{O}_3]_N$ multilayer samples studied. For each superlattice, the thickness of the polycrystalline permalloy layer d_{Py}, the period d (bilayer thickness), the Py volumic fraction f_{Py}, the number N of periods and the total film thickness are given. Additional information is given in the text.

	Multilayer characteristics				
Sample name	Py layer d_{Py} (nm)	Period d (nm)	f_{Py} (%) d_{Py}/d	Number N	Film thickness (nm)
$M1$	1.4	5.3	26.4	30	187.1
$M2$	1.6	5.5	29.1	50	303.1
$M3$	2.4	6.3	38.1	50	343.1
$M4$	2.7	6.6	40.9	30	226.1
$M5$	2.9	6.8	42.6	30	232.1
$M6$	4	7.9	50.6	30	265.1
$M7$	5.7	9.6	59.4	50	508.1
$M8$	7.9	11.8	66.9	30	382.1
$M9$	10.6	14.8	71.6	10	166.4

II. EXPERIMENT

A. Sample preparation and characteristics

The system investigated in this work corresponds to a metal-insulator composite system where a ferromagnetic metallic material (permalloy) is in contact with a dielectric (Al_2O_3) in a layered structure geometry. The permalloy material (hereafter abbreviated by Py) corresponds actually to a NiFe alloy of atomic composition $Ni_{80}Fe_{20}$. Two categories of samples have been studied: (i) a set of "single layer" samples characterized by a *thick* layer of one of the two basic materials (either Py or Al_2O_3); (ii) a set of multilayers $[\text{Py-Al}_2\text{O}_3]_N$, corresponding to the periodic stacking (N periods) of bilayers Py-Al_2O_3 where the thickness of each individual layer lies in the *ultrathin* (nanometric) range.

The samples studied correspond to films which have been elaborated by sputtering. A detailed report on the film preparation and their characterization is given in Ref. 20. In summary, these films have been deposited by rf sputtering, at room temperature, on single crystalline Si (001) substrates. In the sputtering configuration used, the Py target (alloy of atomic composition $Ni_{80}Fe_{20}$) was placed on a rf diode electrode whereas the alumina target (Al_2O_3) was lying on a rf magnetron electrode, in order to enhance the deposited rate of alumina. For all the samples a static mode of sputtering has been used, where the substrate is continuously facing the activated target during deposition. For the very thin layers of Py and Al_2O_3 considered here (in the multilayers), their individual thickness is only monitored in the sputtering process by their time of deposition (measured experimentally). So the individual layer thickness given in Table I correspond merely to a conversion of the actual times of deposition in terms of thickness according to the deposition rates of the two materials. These deposition rates have been determined by thickness measurements performed on thick films and multilayers. They correspond, respectively, to 3.6 ± 0.1 nm/min for Py and 9.3 ± 0.3 nm/min for Al_2O_3.

The characteristics of the samples are as follows: The thick single Py layer sample (labeled P1) that we took as a reference to determine the permalloy bulk properties, corresponds actually to a film having the sandwich structure: (Al_2O_3 base$|$Py$|$$Al_2O_3$ top). The Py layer thickness is 323 nm; the Al_2O_3 base and top are, respectively, 18.4 nm and 9.7 nm thick. For alumina, four single Al_2O_3 layer samples (labeled A1, A2, A3, and A4) have been elaborated. The alumina thickness is respectively 112 nm (A1); 117 nm (A2); 273 nm (A3). Sample A4 corresponds to a very thick film (2450 nm) and has been used as a reliable reference for determining the elastic properties of the bulk amorphous alumina.

The main characteristics of the multilayer samples (labeled $M1$ to $M9$) are summarized in Table I. Each film corresponds to a multilayer $[\text{Py-Al}_2\text{O}_3]_N$ sandwiched by alumina with Al_2O_3 base and top layers having thicknesses identical to the ones in sample P1, except for $M9$ which has no top on it. For all the samples in this series, the Al_2O_3 spacer thickness is $d_{\text{Al}_2\text{O}_3} = 3.9$ nm (slightly different only for $M9$: $d_{\text{Al}_2\text{O}_3} = 4.2$ nm); each sample has a different Py thickness d_{Py}. We indicate in Table I, for each sample, the period $d = d_{\text{Py}} + d_{\text{Al}_2\text{O}_3}$, the volumic fraction of permalloy f_{Py} (defined by $f_{\text{Py}} = d_{\text{Py}}/d$), the number N of periods and the total film thickness. It may be noticed that the period d, for this set of samples, spans the range (5.3—14.8 nm) and that the Py volumic fraction varies correspondingly in the range (26.4%—71.6%).

For an ensemble of films relative to the (Py-Al_2O_3) composite system, a set of x-ray diffraction measurements has been performed: experiments at low angles for multilayers, and at large angles for multilayer and single Py layer samples. A detailed report on these measurements is given in Ref. 20. In summary, the essential results obtained are the following. The permalloy layers are polycrystalline and the alumina is amorphous. At low angles the multipeak diffraction spectra observed in the multilayers, which show in the explored angular range many peaks of monotonic decreasing intensity, reveal a good periodic structure of these multilayers and suggest further that the interfaces are rather sharp (at least for the films deposited at room temperature). The results of the large angle x-ray diffraction measurements indicate that the Py polycrystalline layers (in the 3–11 nm thickness range) have a good (111) texture, single crystallites being formed through the whole layer thickness. They are characterized by a weak disorientation (typically 0.4–0.6°) of the crystallites with respect to the film normal, as deduced from the midheight width of the rocking curve recorded around the (111) Bragg peak.

B. Picosecond ultrasonics

The picosecond ultrasonic technique[21,22] is based on a time-resolved pump-probe setup involving sub-picosecond laser pulses. A first laser pulse, the pump pulse, generates an elastic disturbance in the sample which is subsequently probed by a time delay laser pulse, the probe pulse. The absorption of a pump pulse underneath the illuminated sur-

face sets up a local thermal stress which in turn generates an acoustic field within the material. For a layer onto a substrate, this field results in an elastic pulse bouncing back and forth between the interface and the free surface where it produces acoustic echoes. In superlattices, partial reflections occur at each interface. If, moreover, the stacking is periodic, these reflections add constructively, except for well defined frequency stop bands. Elastic strain pulses with frequencies lying outside these gaps can still propagate along the stacking axis. In addition, stationary modes showing frequencies within the gap may also occur.[9,23–27] The acoustic field induces changes $\Delta r(t)$ in the complex optical reflectivity coefficient r_0 of the structure and thus alters the electromagnetic field of the reflected probe. The amplitude and phase changes of this field can then be probed by an interferometric detection set up.[27–29]

In our apparatus, optical pulses with a duration of 130 fs and a typical energy of a few nJ are generated by a Ti: sapphire laser working at 750 nm with a 82 MHz repetition rate. The pump beam is modulated at a frequency of 1 MHz. The probe pulses can be delayed with respect to the pump pulses up to a few nanoseconds by means of a variable optical path and are detected by a lock-in amplifier at the 1 MHz pump modulation frequency.

In the experiments described here, the pump beam was focused onto a spot having a diameter of roughly 30 μm which is much larger than the optical absorption length of the multilayer structure (tens of nm). Consequently, a onedimensional model (along the stacking direction z) can be used to describe both the elastic waves generation and the detection processes; only longitudinal waves have to be considered.[21]

The relative change in reflectivity was calculated in a previous article[28] and the main results are recalled here. Let a structure made of M layers indexed by m, in between a cap layer ($m=1$) and the substrate ($m=M+1$). d_m is the thickness of the layer m. A local coordinate z, defined within each layer, is running from 0 to d_m. The electromagnetic field in the layer m, can be written as the sum of two counter propagating plane waves:

$$E_m(z) = a_m e^{ik_m z} + b_m e^{-ik_m z}, \tag{1}$$

where $k_m = \sqrt{\varepsilon_m} k_0$; ε_m is the dielectric constant and k_0 is the optical wave vector in vacuum. The reflection coefficient $r_0 = a_0/b_0$ of the whole structure can be related to the amplitudes (a_m, b_m) of the forward and backward electromagnetic fields. These can be calculated using a transfer-matrix formalism. The probe pulse is affected by the acoustic field propagating within a layer in two respects: on the one hand, each interface is displaced by the acoustic wave; on the other hand, the dielectric constant is modified by the elastic strain η. The relative change of reflectivity is thus the sum of these two contributions and can be written as

$$\frac{\Delta r}{r_0}(t) = \frac{ik_0}{n_0 a_0 b_0} \sum_{m=0}^{M+1} \left\{ 2\varepsilon_m a_m b_m (u_m(t) - u_{m-1}(t)) + \frac{1}{2}\frac{\partial \varepsilon_m}{\partial \eta} \int_0^{d_m} dz\, \eta_m(z,t) [a_m e^{ik_m z} + b_m e^{-ik_m z}]^2 \right\}, \tag{2}$$

with $d_{M+1} \to +\infty$, $\partial \varepsilon_0 / \partial \eta = 0$, and $u_{-1}(t) = 0$; $\partial \varepsilon_m / \partial \eta$ and u_m are, respectively, the photoelastic coefficient and the normal acoustic displacement in the layer m. This relative change of reflectivity is a complex quantity which can be expressed as $\Delta r(t)/r_0 = \mathrm{P}(t) + i\Phi(t)$, where, since $10^{-7} \leqslant \Delta r(t)/r_0 \leqslant 10^{-3}$, $P(t)$ and $\Phi(t)$, stand for the amplitude relative change and phase change of the reflected electromagnetic beam respectively. Both the real and the imaginary parts, $P(t)$ and $\Phi(t)$, can be obtained through the interferometric detection.

To use Eq. (2), the acoustic field, namely $u_m(t)$ and $\eta_m(z,t)$, must be determined within each layer. This is a complex task since each individual layer acts as an acoustic source as far as the pump beam penetrates in the structure and the fields generated by these many sources propagate and superimpose. The problem can be solved in the frequency domain expanding the acoustic field in term of stationary waves within each layer

$$u_m(z,t) = A_m e^{iq_m z} + B_m e^{-iq_m z}, \tag{3}$$

where A_m and B_m are the complex amplitude of counter propagating acoustic waves in the layer m and $q_m = \omega / v_m$ is the acoustic wave vector. Using a transfer matrix formalism, A_m and B_m can be expressed in terms of A_{m-1} and B_{m-1} and of the acoustic source in the layer m due to the absorption of the pump pulse. We performed numerical simulations according to this scheme which will be discussed in the following section.

The problem of acoustic propagation in multilayers when the acoustic sources are neglected is much simpler and the main results are summarized below.[23]

For a layer with a thickness d, and an acoustic impedance $Z = \rho v$, we define the transfer matrix τ, for the normal component of the displacement u and the relevant stress tensor component σ, by

$$\begin{pmatrix} u_R \\ \sigma_R \end{pmatrix} = \tau \begin{pmatrix} u_L \\ \sigma_L \end{pmatrix} = \begin{pmatrix} \cos(qd) & \sin(qd)/\omega Z \\ -\omega Z \sin(qd) & \cos(qd) \end{pmatrix} \begin{pmatrix} u_L \\ \sigma_L \end{pmatrix}, \tag{4}$$

where the indices L and R stand, respectively, for the left and right-hand sides of the layer. In the long wavelength limit, i.e., $dq \ll 1$, the transfer matrix τ simply reduces to

$$\tau = \begin{pmatrix} 1 & d/C_{33} \\ 0 & 1 \end{pmatrix}, \tag{5}$$

where $C_{33} = \rho v^2$.

If, both, continuity of u and σ is assumed at the interface, the transfer matrix τ for a superlattice with the period d is then equal to the product $\tau_2 \tau_1$ of the respective transfer matrices of the constitutive layers 1 and 2 of thickness d_1 and d_2. The effective elastic constant C_{33} of the superlattice is thus given by the simple relation

$$\frac{d}{C_{33}} = \frac{d_1}{C_{33}^{(1)}} + \frac{d_2}{C_{33}^{(2)}}, \tag{6}$$

where $d = d_1 + d_2$ is the repeat distance. This relation is only valid in the limit where the acoustic wavelengths are much longer than the period of the superlattice d.

The determinant of τ being equal to 1, its eigenvalues can be written (e^{iqd}, e^{-iqd}); q turns out to be the effective wave vector of the superlattice. The trace of τ gives the dispersion relation for longitudinal modes propagating along the stacking axis of an infinite multilayer,

$$\cos(qd) = \frac{1}{2}\,\mathrm{Tr}(\tau) = \cos(q_1 d_1)\cos(q_2 d_2) - \frac{1}{2}\left(\frac{Z_1}{Z_2} + \frac{Z_2}{Z_1}\right)\sin(q_1 d_1)\sin(q_2 d_2). \tag{7}$$

As long as $|\cos(qd)| < 1$, this dispersion relation defines propagating modes with an effective sound velocity in the long wavelength limit. Frequencies that would correspond to values of $|\cos(qd)| \geqslant 1$ in Eq. (7), define band gaps in the dispersion curves in which no propagating modes are allowed. These band gaps arise at the center $(q = 0 \pm 2n\pi/d)$ and at the boundary $(q = \pi/d \pm 2n\pi/d)$ of the superlattice Brillouin zone.

For semi-infinite superlattices, localized modes can exist, with frequencies lying in the acoustic band gaps. They correspond to vibrations confined within the very first periods of the multilayer. The frequencies of these modes are determined by the requirement that $\binom{u}{0}$ is an eigenvector of the transfer matrix τ (stress-free limit condition), namely,

$$\tau \begin{pmatrix} u \\ 0 \end{pmatrix} = \lambda \begin{pmatrix} u \\ 0 \end{pmatrix}, \tag{8}$$

with $|\lambda| < 1$. One can show[23,24] that this condition implies that the material at the free surface of the superlattice has a smaller acoustical impedance than the underlying one.

When a cap layer covers the superlattice, the vector $\tau_C \binom{u}{0}$ should be substituted to $\binom{u}{0}$ in Eq. (8), where τ_C is the cap layer transfer matrix. No simple condition for the existence of localized modes can be found in that case. When the effective optical absorption length is longer than the period of the superlattice, it can be shown[29,30] that localized surface modes in the first zone center band gap $(q = 2\pi/d)$ are preferably excited and more efficiently detected. For larger periods, localized modes in the first zone-boundary band gap $(q = \pi/d)$ can also be observed.

Besides the measurement of the time of flight of an acoustic pulse propagating in the whole multilayer, pieces of information about the acoustic properties of the superlattice can also be obtained from the experimental determination of the localized surface modes frequencies. Indeed, whereas the former measurement allows to characterize the effective medium (effective sound velocity and effective elastic constants), the latter is related to the elastic parameters of each constitutive layer.

C. Brillouin light scattering

Room temperature Brillouin spectra were recorded using a Sandercock type tandem 2×3 pass Fabry-Pérot interferometer[31] with a typical finesse of about 100 and a contrast ratio higher than 10^{10}. A *p*-polarized illuminating beam at 514.5 nm wavelength, emitted by a single mode Ar^+ laser, was focused on the surface of the samples. The backscattering geometry was chosen for recording the spectra: the angle of incidence θ could be experimentally monitored, allowing thus to probe various surface wave vectors $Q_\parallel$ of the surface excitations ($Q_\parallel = 2k \sin\theta$, where k denotes the optical wave vector of the light) in the range of a few 10^{-2} nm^{-1} (wavelength typically around 300 nm). The incident power did not exceed 300 mW, thus limiting the sample heating. Notice that the magnetic character of permalloy leads to magnon scattering in addition to the phonon spectra under the present study: magnon lines are only observed in s polarization while the scattered surface phonons appear principally, but not exclusively, in *p* polarization. In order to improve the collected intensity, most of the spectra were performed without analyzing the scattered polarization: an appropriate magnetic field was applied in order to shift the magnon scattering out of the frequency range of the studied phonon surface modes. With the above-described experimental conditions the time of acquisition was generally of 2 or 3 h per recorded spectrum.

For opaque materials the Brillouin scattering originating from the surface elastic waves mainly arises from a ripple mechanism[32] which leads to *p*-*p* (and *s*-*s*) polarization selection rules; consequently, it is not observable using cross *p*-*s* (or *s*-*p*) polarizations, in contrast with the magnon scattering. However, in transparent materials, there is an additional contribution to the phonon scattering related to the photoelastic coupling.[33–35]

The analysis of the spectra, based on the elastic continuum theory of a multilayered structure on a cubic substrate,[36] can be performed using a Green function approach of the equations of motion with appropriate boundary conditions; generally, one evaluates the spectral density of the surface displacements $u_z = 0$ at the free surface[32] and at the interfaces, which allows to calculate the shapes of the Brillouin spectra when neglecting the photoelastic contribution. For opaque samples these spectra only depend upon the displacements of the free surface. In transparent structures the ripple mechanism involves several interfaces: in such cases, our intensity calculations include these interfering contributions. Moreover, in principle, for a complete quantitative interpretation, one has to take account of the photoelastic coupling; this can also be performed by the Green function approach[37] but is not fully developed in the present article.

III. EXPERIMENTAL RESULTS AND DISCUSSION

A. Picosecond ultrasonics results

We describe in this section our picosecond ultrasonics results and we compare them to the analytical calculation of the relative reflectivity changes $\Delta r(t)/r_0$. We have first measured the elastic parameters of single layer samples in order to obtain the reference values for the elastic parameters of amorphous alumina and polycrystalline permalloy. Indeed, the elastic properties of sub-micrometric layers can be different from the bulk, making essential this preliminary work. We then report on the measurements of the effective elastic

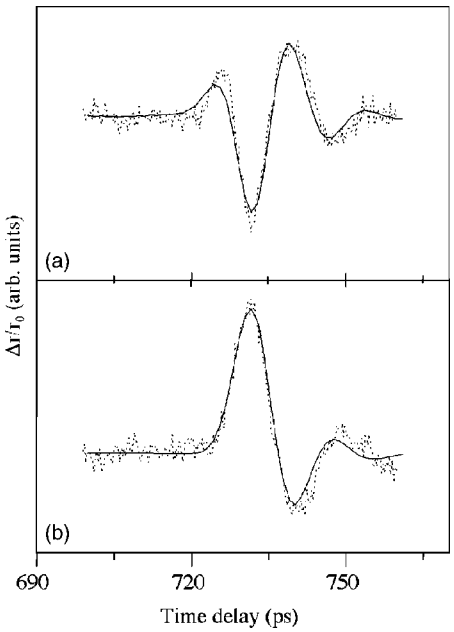

FIG. 1. Real (a) and imaginary (b) parts of the relative variation of the reflectivity $\Delta r(t)/r_0$ observed in an amorphous alumina layer A4 ($d_{Al_2O_3}=2450$ nm) capped with a pure aluminum layer $d_{Al}=15$ nm. The thermal background has been subtracted and only the first acoustic echo is shown. The dots are the experimental results, and the solid line the theoretical expectations (calculations described in the text).

parameters of the multilayers and we compare them to the ones expected from the reference values. Finally, the effect of modified interfaces on the effective elastic response is discussed.

1. Single layer samples

The thickness d of our samples being known with an excellent accuracy, the longitudinal sound velocities in alumina and permalloy can be deduced from the measurement of the time T separating two consecutive acoustic echoes, using $v=2d/T$. The longitudinal elastic constant $C_{33}=\rho v^2$ can be calculated in turn from both the sound velocity and the density. In order to reduce the uncertainty originating from the finite duration of an elastic echo, we have analyzed in detail the shape of each echo. For that purpose we have developed a simulation program[38] which allows to calculate both the real and the imaginary parts of the reflectivity changes resulting from the alteration of optical, thermal and acoustical properties of an illuminated layered sample. We applied the procedure to sample A1 to A4 and P1. However, sample P1 being covered with an alumina cap layer, the determination of the longitudinal elastic constant of Py requires the prior knowledge of the longitudinal elastic constant of Al_2O_3.

Amorphous alumina. Alumina being transparent for the wavelength of our laser, sample A4 ($d_{Al_2O_3}=2450$ nm), the sample was covered by a thin metallic aluminum cap layer ($d_{Al}=15$ nm) acting as an acoustic transducer.[22] In Fig. 1 are displayed the real (a) and the imaginary (b) parts of the reflectivity change arising from the first acoustical echo in sample A4. The thermal background has been subtracted. A standard nonlinear least squares fitting routine was used to account for data over the range from 700 to 760 ps. The agreement between experimental and theoretical results is excellent. The best fit to the data, using the bulk density $\rho_{Al_2O_3}=3.95\pm0.1$ g/cm^3 and the refractive index $n_{Al_2O_3}=1.6\pm0.2$ determined by ellipsometry, yields the longitudinal sound velocity $v_{Al_2O_3}=6.7\pm0.2$ nm/ps. The corresponding elastic constant is then $C_{33}^{(Al_2O_3)}=\rho_{Al_2O_3}v_{Al_2O_3}^2=178\pm5$ GPa and is reported in Table II. The results obtained with the three other samples A1–A3 are very similar and are not detailed in this article. However, these samples being not covered with an aluminum cap layer, the pump pulse is absorbed by the silicon substrate. As a consequence of the large optical absorption length in this material the acoustic spectrum extends to lower frequencies leading to a smaller accuracy.

TABLE II. Elastic constants of the amorphous alumina and of the polycrystalline permalloy single layers derived from the picosecond ultrasonics and the Brillouin light scattering measurements. The Voigt and Reuss estimated values (Refs. 46 and 47) of the elastic constants for a bulk ⟨111⟩ textured polycrystalline permalloy are also reported for comparison in the last line.

		Brillouin light scattering				Picosecond ultrasonics
Material	ρ(g cm^{-3})	C_{11} (GPa)	C_{33}	C_{44}	C_{13}	C_{33}
Al_2O_3	3.95±0.1	176±3	C_{11}	53±1	C_{12}	178±5
Py	8.69±0.1	265±10	275[a]	66±3	140±5	275±5
				Voigt [Reuss][b]		
		306 [287]	331 [331]	68 [55]	93 [93]	331 [331]

[a]Value taken from picosecond ultrasonics measurements.
[b]Reference 46 and 47.

Polycrystalline permalloy. We have plotted in Fig. 2 the real (a) and the imaginary (b) parts of the reflectivity change in sample P1 (only the two first echoes are displayed). The thermal background was subtracted in order to allow comparison with numerical simulations. These echoes originate from the strain pulse created in the Py film and are reflected at the Al_2O_3 base/-Si interface; then, they are detected both in the alumina top and in the Py layer. Again, a standard nonlinear least squares fitting routine was used to analyze data over the range from 75 to 275 ps. The reflectivity change, calculated using $v_{Py}=5.6\pm0.2$ nm/ps and $\rho_{Py}=8.69\pm0.1$ g/cm^3 (deduced from x-ray diffraction measurements), satisfactorily fits our experimental data. The calculation takes into account alumina base and top in P1. The elastic constant of permalloy is then $C_{33}^{(Py)}=\rho_{Py}v_{Py}^2=275\pm5$ GPa (see Table II). The refractive index of permalloy was also deduced from the fit of the acoustic echoes. We found $n_{Py}=(2.5\pm0.2)+(4.1\pm0.2)i$ which is in between the values of bulk nickel and iron, namely, $2.35+4.24i$, and $2.99+3.56i$, respectively.[39]

Knowing the elastic parameters for amorphous alumina ($C_{33}^{(Al_2O_3)}=178\pm5$ GPa) and for polycrystalline permalloy

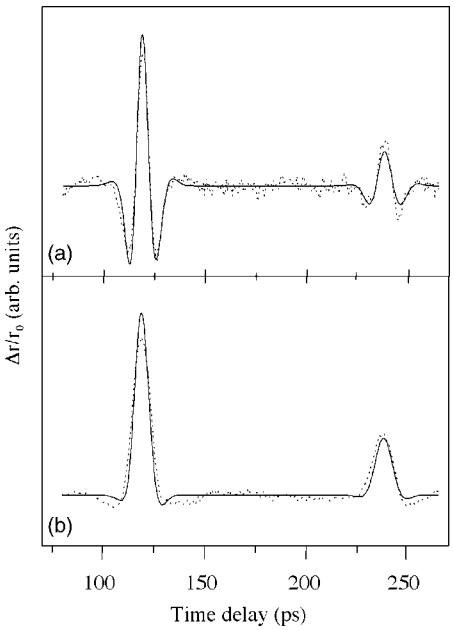

FIG. 2. Real (a) and imaginary (b) parts of the relative variation of the reflectivity $\Delta r(t)/r_0$ observed in a polycrystalline permalloy layer P1 (d_{Py}=323 nm). The thermal background has been subtracted and the two first echoes are shown. The dots are the experimental results, and the solid line the theoretical expectations (calculations described in the text).

($C_{33}^{(Py)}$=275±5 GPa) films, we are now able to analyze our results obtained on superlattices.

2. Multilayers

We have studied the set of periodic multilayers Py-Al_2O_3 described in Table I and labeled $M1-M9$. The period of these multilayers varies from 5.3 to 14.8 nm. The material at the free surface is amorphous alumina for all the samples, except $M9$ for which the last stacked layer is permalloy. All the recorded signals exhibit, over the first hundreds of picoseconds, several acoustic echoes originating from a strain pulse which propagates through the whole superlattice, and is reflected between the interface with the substrate and the free surface where it is detected at constant time intervals (Fig. 3). In addition, some samples ($M1$, $M4$, $M6$, $M7$, and $M8$) show over the first tens of picoseconds damped oscillations originating from localized surface modes (Fig. 3).

In order to determine the effective sound velocities we compared the experimental results with numerical simulations. The effective elastic constant is obtained using the simple relation $C_{33}=\rho v^2$, where ρ is the effective density defined by $d\rho=d_1\rho_1+d_2\rho_2$. The result is reported in Fig. 4. For comparison, we have displayed in the same figure the effective elastic constant C_{33} derived from Eq. (6), using the reference elastic parameters of permalloy and alumina (Table II). Whatever the Py layer thickness in the superlattice, the measured elastic constant is smaller than the expected value, attesting a strong softening of the superlattice. The discrepancy is about 7% for the sample with the largest Py layer

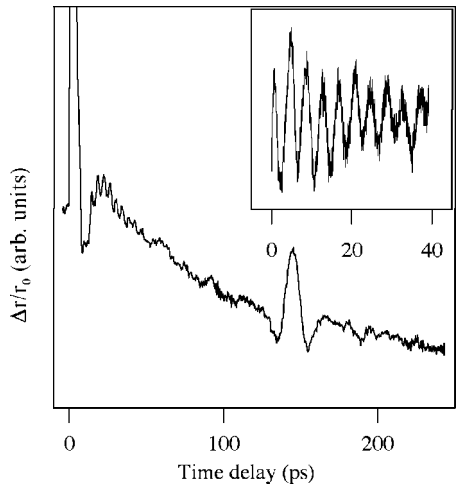

FIG. 3. Real part of the relative variation of the reflectivity $\Delta r(t)/r_0$ observed in a multilayer sample $M8$ (d_{Py}=7.9 nm). The inset, where the thermal background signal has been subtracted, displays the localized mode (250 GHz) observed in the short time delay range.

thickness and rises up to 40% for the thinnest Py layer thickness.

Two possible causes can be at the origin of these elastic anomalies. One is the alteration of the elastic properties due to variations of the composition and/or densities of both materials. However, it is not likely to explain such a strong variation of the effective elastic constant since it would imply density variations up to 40%. Another explanation is the occurrence of interfacial effects between Py and Al_2O_3 thin films. Actually, electronic effects cannot be suspected in this metal-insulator system, in contrast with the case of metal-metal multilayers.[40] On the other hand, a similar softening of the longitudinal elastic constant has already been observed in

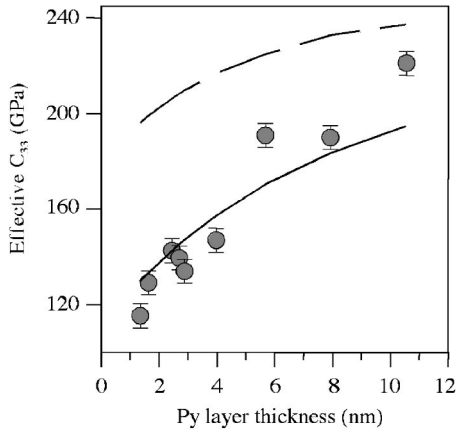

FIG. 4. Variation of the effective longitudinal elastic constant C_{33} (GPa) of the bilayer permalloy-alumina as a function of the Py layer thickness in the superlattice. Experimental results (circle dots) show a strong softening, from 7% up to 40%. The broken line comes from the perfect interfacial bonding model with the reference single layers properties. The solid line is the best fit for modified interfaces models: Py volume inhomogeneity model or weak interfacial bonding model.

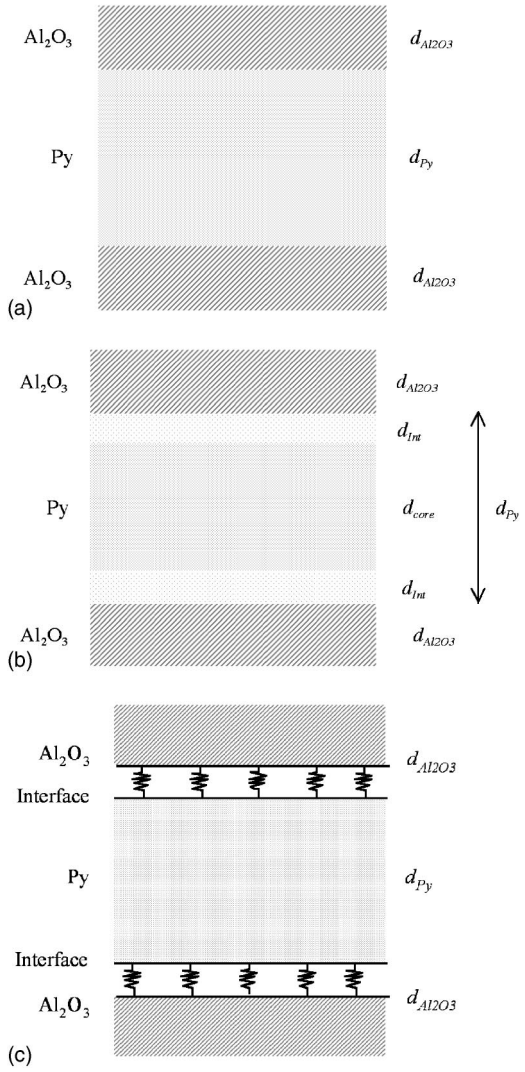

FIG. 5. Schematic diagrams of the interfacial models: (a) M_A: perfect interfacial bonding model, (b) M_B: Py volume inhomogeneity model, (c) M_C: weak interfacial bonding model.

the metal-insulator system AlN-ZrN and was interpreted in terms of a crystalline to amorphous structural transition when the bilayer thickness decreases.[17] However, in agreement with expectation based on electronic arguments, no such changes were observed in the metal-insulator superlattice AlN-NbN.[18] To account for the observed softening of C_{33}, two phenomenological models are therefore suggested. The first modified model, hereafter noted M_B, assumes a volume inhomogeneity of permalloy whereas the second one, M_C, is based on the weakness of the bonding between two adjacent layers.

Model M_A: Perfect interfacial bonding: Under such an assumption, the elastic constant and the density of each material are independent of the layer thickness. The bonding at the interface is supposed to be perfect [Fig. 5(a)], implying continuity of both the acoustic displacement and the stress. The effective elastic constant C_{33} of the Py-Al_2O_3 bilayer is simply given by Eq. (6),

$$\frac{d}{C_{33}} = \frac{d_{\mathrm{Al_2O_3}}}{C_{33}^{(\mathrm{Al_2O_3})}} + \frac{d_{\mathrm{Py}}}{C_{33}^{(\mathrm{Py})}}. \tag{9}$$

Model M_B: Permalloy volume inhomogeneity: In this model, each permalloy layer is divided in three sublayers [Fig. 5(b)]: two interfacial zones [thickness d_{Int} and elastic constant $C_{33}^{(\mathrm{Int})}$] embedding a permalloy core, the thickness and elastic constant of which are, respectively, $d_{\mathrm{core}}=d_{\mathrm{Py}}-2d_{\mathrm{Int}}$ and $C_{33}^{(\mathrm{Py})}$. We assume that densities of the core and interfacial zones are identical and equal to ρ_{Py}; $C_{33}^{(\mathrm{Py})}$ and ρ_{Py} are the values deduced from the thick single layer samples. We further suppose that the thickness d_{Int} of the interfacial layer is the same for all the studied samples. Within such a layered structure, the effective constant C_{33} of the Py -Al_2O_3 bilayer is given by

$$\frac{d}{C_{33}} = \frac{d_{\mathrm{Al_2O_3}}}{C_{33}^{(\mathrm{Al_2O_3})}} + \frac{d_{\mathrm{Py}}}{C_{33}^{(\mathrm{Py})}} + 2d_{\mathrm{Int}}\left(\frac{1}{C_{33}^{(\mathrm{Int})}} - \frac{1}{C_{33}^{(\mathrm{Py})}}\right). \tag{10}$$

Model M_C: Weak interfacial bonding: In the framework of this model, we consider that the two media are connected by a massless spring characterized by a strength per unit area ε^{-1} [Fig. 5(c)]. In that case there is no more continuity of the acoustic displacement at the interface. As a consequence of this discontinuity one must define a transfer matrix τ_ε to relate both sides of the interface

$$\begin{pmatrix} u_R \\ \sigma_R \end{pmatrix} = \tau_\varepsilon \begin{pmatrix} u_L \\ \sigma_L \end{pmatrix} = \begin{pmatrix} 1 & \varepsilon \\ 0 & 1 \end{pmatrix} \begin{pmatrix} u_L \\ \sigma_L \end{pmatrix}. \tag{11}$$

Considering the long wavelength limit of the period transfer matrix, it is straightforward to show that the effective elastic constant C_{33} of the bilayer is

$$\frac{d}{C_{33}} = \frac{d_{\mathrm{Al_2O_3}}}{C_{33}^{(\mathrm{Al_2O_3})}} + \frac{d_{\mathrm{Py}}}{C_{33}^{(\mathrm{Py})}} + 2\varepsilon. \tag{12}$$

A similar model was introduced by Tas *et al.*[15] to investigate the modification of the interfacial bonding resulting from ion implantation.

It is interesting to notice that model M_B is characterized by two parameters, d_{Int} and $C_{33}^{(\mathrm{Int})}$, whereas model M_C involves only one parameter, namely ε. Moreover, M_B and M_C lead to an identical dependence of the effective constant C_{33} in terms of the Py layer thickness d_{Py},

$$\frac{d}{C_{33}} = \frac{d_{\mathrm{Al_2O_3}}}{C_{33}^{(\mathrm{Al_2O_3})}} + \frac{d_{\mathrm{Py}}}{C_{33}^{(\mathrm{Py})}} + 2\Omega \tag{13}$$

with

$$\Omega = \varepsilon = d_{\mathrm{int}}\left(\frac{1}{C_{33}^{(\mathrm{Int})}} - \frac{1}{C_{33}^{(\mathrm{Py})}}\right). \tag{14}$$

The best fit to the data using Eq. (13) is displayed in Fig. 4; we found $\Omega = 6.7 \pm 0.2 \times 10^{-3}$ nm GPa^{-1}.

For model M_B, only a relation, Eq. (14), between the thickness of the extended interface d_{Int} and the elastic constant $C_{33}^{(\mathrm{Int})}$ can be deduced. Concerning model M_C, the strength $(1/\varepsilon = \Omega^{-1})$ of the massless spring is 149 ± 5 GPa/nm.

TABLE III. Frequencies of measured and calculated localized modes. Parameters used in the calculation are given in the text.

Multilayers	Experiments (±10 GHz)	Interfacial models		
		Model M_A[a]	Model M_B[b]	Model M_C[c]
	First zone center band gap localized modes frequencies (GHz)			
$M1$	980	1150	982	834–1050
$M4$	790		799	810
$M6$	660		620	624
$M7$	590	633	572	564
	First zone boundary band gap localized modes frequencies (GHz)			
$M1$	480	623	474	473
$M8$	250		250	252

[a]Model M_A: perfect interfacial bonding.
[b]Model M_B: Py volume inhomogeneity model.
[c]Model M_C: weak interfacial bonding.

Additional information can be obtained from the frequencies of the localized surface modes. The frequencies, deduced from Fourier transform of the relevant part of the signal, are summarized in Table III. They range from 250 ± 10 GHz for the largest period (sample $M8$) up to 980 ± 10 GHz for the smallest one (sample $M1$). Vibrations localized either in the first zone center acoustic band gap ($M1$, $M4$, $M6$, and $M7$) or in the first zone boundary acoustic band gap ($M1$ and $M8$) are observed. The photoelastic response of sample $M1$ is particularly interesting since it consists of two vibrations localized in the two first band gaps. No localized mode was observed in $M2$, $M3$, and $M5$ samples.

The frequencies of the localized modes can be calculated for the three models using three different transfer matrices:

$$\tau_A = \tau_{\mathrm{Py}}\tau_{\mathrm{Al_2O_3}}, \tag{15}$$

$$\tau_B = \tau_{\mathrm{Int}}\tau_{\mathrm{Py}}\tau_{\mathrm{Int}}\tau_{\mathrm{Al_2O_3}}, \tag{16}$$

and

$$\tau_C = \tau_{\varepsilon}\tau_{\mathrm{Py}}\tau_{\varepsilon}\tau_{\mathrm{Al_2O_3}}. \tag{17}$$

Results of the calculations are reported in Table III.

It clearly appears from the comparison between measured frequencies and values predicted by model M_A, that the assumption of a perfect bonding at each interface does not hold: some localized modes should not exist in samples $M4$, $M6$, and $M8$ where they are actually observed; in samples $M1$ and $M7$ where a localized mode is predicted by model M_A, and effectively observed, there is a large discrepancy between the theoretical and the measured frequency.

We have studied the dependence of the frequency of the localized modes as a function of the interface thickness d_{int}, in the range 0.1–0.675 nm, in the framework of model M_B. To this end, we have assumed that for each value of d_{int}, $C_{33}^{(\mathrm{Int})}$ is deduced from Eq. (14) using $\Omega=6.7\pm0.2\times10^{-3}$ nm GPa^{-1}.

The results for the first zone centre localized mode in the thinnest period multilayer $M1$ are displayed in Fig. 6. Dashed lines (a) and (d) correspond, respectively, to the upper and lower edges of the band gap which disappears for this sample when the thickness of the interfacial layer reaches 0.7 nm. Full lines (b) and (c) correspond to two localized modes which coexist within the same gap for an interface thickness up to $d_{\mathrm{Int}}=0.4$ nm. Beyond this value and up to $d_{\mathrm{Int}}=0.57$ nm, a single localized mode at a frequency close to the experimental one subsists. Vertical dotted lines in Fig. 6 delimit two intervals: from 0 to line (e) both localized modes (b) and (c) are allowed, whereas only the upper one (b) holds between (e) and (g). For this sample, the two values, $d_{\mathrm{Int}}=0.34$ nm and $d_{\mathrm{Int}}=0.57$ nm define a realistic interval for the thickness of the extended interface.

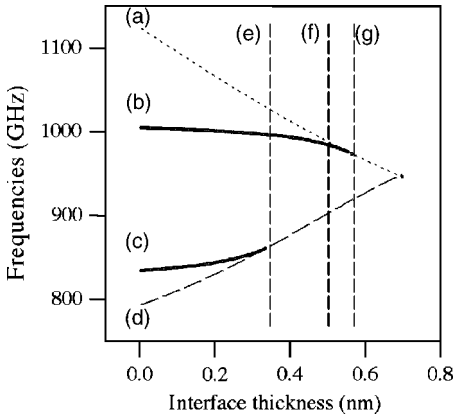

FIG. 6. Calculated frequencies of the zone center localized modes (b) and (c) shown with solid lines, as a function of the interfacial layer thickness d_{Int} within the interfacial model M_B (Py volume inhomogeneity). The dotted line (a) and broken line (d) correspond to the upper and lower band edges of the first zone center gap, respectively. Vertical broken lines (e) and (g) define the thickness interval (0.34–0.57 nm) for which calculated frequencies are close to the experimental one (980 ± 10 GHz), and the vertical broken line (f) stands for the best fit (0.52 nm–982 GHz).

We did the same study for the other samples exhibiting oscillations ($M4$, $M6$, $M7$, and $M8$) with a thickness of the interfacial layer varying in this interval (0.34 nm–0.57 nm). The overall best agreement with the experimental data was obtained for $d_{\mathrm{Int}}=0.52$ nm ($C_{33}^{(\mathrm{Int})}=60.5$ GPa). Line (f) in Fig. 6 corresponds to this value for sample $M1$. Frequencies calculated with this value are given in Table III. They differ from the experimental frequencies by less than 2%, except for the sample $M6$ where the discrepancy is about 5%.

Finally the frequencies of the localized modes have also been calculated in the framework of the model M_C with the value $\varepsilon=6.7\pm0.2\times10^{-3}$ nm GPa^{-1}. For samples $M4$, $M6$, $M7$, and $M8$ the model predicts a single localized mode. The discrepancy with experimental results is larger than for model M_B. Furthermore, in the thinnest period sample $M1$, two localized modes with respective frequencies 834 and 1050 GHz, far from the experimental value of 980 GHz, are predicted.

Consequently model M_B is in better agreement with the experimental results and seems more relevant to explain the strong elastic constant softening that we observed.

At this stage it appears appropriate, by comparison, to mention and quote briefly results (and analysis) of magnetization measurements described in detail in Ref. 20. Systematic magnetization measurements have been performed on different series of single ultrathin Py layers (sandwiched by Al_2O_3). A thickness dependence of the saturation magnetization M_s is observed for d_{Py} in the range 2–11 nm. These results have been reasonably well accounted for in terms of a volume magnetic inhomogeneity model for the permalloy layer. In this model one considers that the magnetic layer is composed of basically two zones of different magnetization: an interfacial layer (thickness d_{Int}, assumed constant along a sample series, and magnetization M_{Int}) and a "core" layer (thickness d_{core}, magnetization M_{core}). One derives from the analysis that M_{core} corresponds well to the M_{Py} bulk value expected for a $Ni_{80}Fe_{20}$ alloy (target composition), and actually measured in thick Py layers. A number of physical reasons may be responsible for the fact that M_{Int} is different from M_{core}. The main ones would be the following: (i) local variation of the atomic composition of the NiFe alloy; (ii) intrinsic variation of the magnetic moment of Ni atoms at the interface; (iii) effects induced by roughness and local atomic disorder.

B. Brillouin light scattering

In the following we describe the results on Al_2O_3 and Py single layer samples and on multilayer samples.

1. Single layer samples

The elastic constants of amorphous alumina (isotropic symmetry) were determined by fitting the surface modes of the four alumina single layer samples (A1–A4), studied for various angles of incidence. The Rayleigh evanescent mode is observed in all the samples while Sezawa and longitudinal guided modes appear well only in the spectra of the 273 nm thick layer (A3). A typical spectrum is shown in Fig. 7: it is compared to the calculated ones, which satisfactorily provide

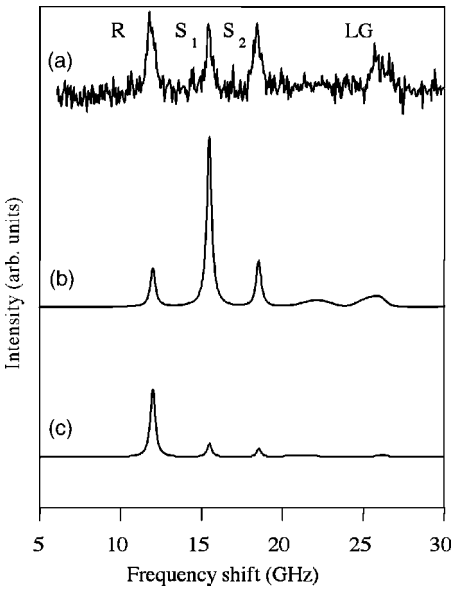

FIG. 7. (a) Experimental Brillouin spectrum of the Al_2O_3 single layer sample A3 (273 nm) compared to the calculated one (b) taking into account the ripple scattering by the two interfaces air-Al_2O_3 and Al_2O_3-silicon, (c) only the ripple scattering from the free surface air-Al_2O_3.

the experimentally measured frequencies. We do not observe standing longitudinal resonances, which can only be activated by the elasto-optic coupling, and which, when they are detected, extend up to high frequencies with a characteristic alternate vanishing.[41] A refractive index of 1.8, determined by ellipsometry measurements at a 546 nm wavelength, was used for the intensity calculations. In Fig. 7, the computed curve (b) takes into account the ripple scattering from both the free surface and the film substrate, whereas the curve (c) includes only the ripple originating from the free surface: the relative intensities of the expected lines significantly differ, but, due to the above-mentioned restriction to the ripple mechanism, the calculations do not reproduce the experimentally observed intensity ratios. To summarize, the elasto-optic coupling is not strong enough to allow the detection of modes forbidden in the approximation of ripple scattering, but it non-negligibly modifies the intensity of the lines allowed through this ripple mechanism. Taking advantage of the whole experimental data and assuming a density equal to 3.95 g/cm^3, we find $C_{11}=C_{33}=176$ GPa and $C_{44}=53$ GPa. Our determination of the longitudinal elastic constant well agrees with the results of picosecond experiments as displayed in Table II.

To determine the effective elastic constants of permalloy, we have studied the reference Py single layer sample (323 nm). In Fig. 8 a typical experimental spectrum is compared to the fitted one: the calculation assumes a ripple mechanism restricted to the free surface and uses the above-determined elastic constants of alumina. The Py density (8.69 g cm^{-3}) was independently deduced from x-ray diffraction data. A preliminary fit was performed assuming an isotropic behavior, leading to $C_{11}=250$ GPa and $C_{44}=63$ GPa.[37] A more satisfactory determination takes into account the appropriate hexagonal symmetry resulting from the averaging

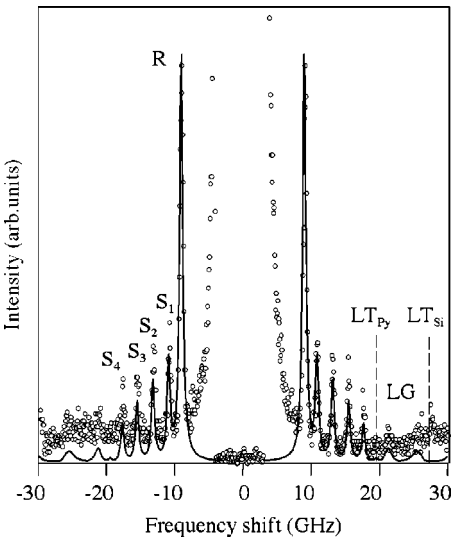

FIG. 8. Comparison between calculated (full line) and measured (dots) Brillouin spectra for the permalloy single layer sample P1 (323 nm) with an angle of incidence of 65°. The Rayleigh surface mode (R), four so-called Sezawa modes (S_i) and two longitudinal guided modes (LG) are present. LT_{Py} and LT_{Si}, are, respectively, the longitudinal threshold frequency of permalloy (19.45 GHz) and silicon (26.85 GHz).

of the in-plane orientations: it provides $C_{44}=66\pm3$ GPa but, due to the increased number of elastic constants to evaluate, it actually contains large uncertainties on the remaining stiffness values. To overcome this problem (at least partly) we used the value $C_{33}=275$ GPa derived from picosecond ultrasonics determination (and, incidentally, close to our 250 GPa result using an isotropic model). Furthermore, this procedure is validated by the good agreement of the fit with the positions of the hardly but undoubtedly detected longitudinal guided modes (LG, above the longitudinal threshold LT_{Py}, see Fig. 8) which strongly depend upon C_{11}. At this stage, it is important to notice that the autocorrelation function of the normal displacement shows small maxima in the vicinity of the frequencies of these LG modes and that, consequently, the ripple mechanism is able to induce scattering from LG modes: such a behavior has been observed and related previously.[42–45] The resulting values for the constants determined by our final fit are collected in Table II. They are compared with the values calculated from the stiffness constants reported in bulk permalloy[46] using Reuss or Voigt averages[47] in order to take account of the random orientation in the films: the agreement is good for the shear constant C_{44} [66 GPa to compare to the (55,68) GPa interval generated by Reuss and Voigt approximations] but it is rather poor for C_{11}, C_{33}, and C_{13}.

2. Multilayers

The multilayer samples were studied systematically. All their Brillouin spectra show at least a line related to the Rayleigh mode. Its variation from sample to sample allows to deduce the dependence of C_{44} versus the Py volumic fraction and, eventually, versus the period of the multilayer. The variation versus d_{Py} is displayed in Fig. 9. This experimentally observed variation is compared to the calculated one using the effective medium approach of a perfect pseudo periodic structure,[48]

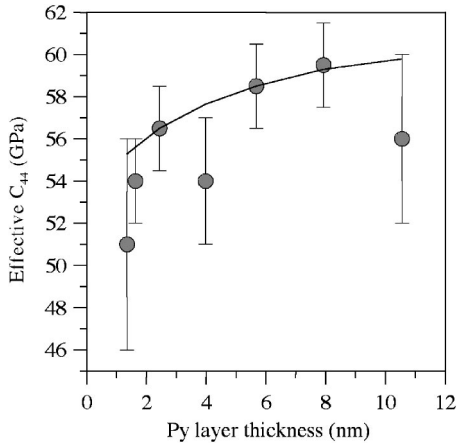

FIG. 9. Variation of the shear elastic constant C_{44} of the Py-Al_2O_3 bilayer versus the Py layer thickness in the superlattice. The circular dots correspond to the experimental determination and the solid line stands for the calculated value using the effective medium approach for a perfect stacking multilayer.

$$C_{44}=\frac{d_{Py}}{d}C_{44}^{(Py)}+\left(1-\frac{d_{Al_2O_3}}{d}\right)C_{44}^{(Al_2O_3)}. \tag{18}$$

We find that, taking account of the uncertainties of their determinations, the above obtained values of $C_{44}^{(Py)}$ and $C_{44}^{(Al_2O_3)}$ provide a satisfactory agreement between the experimental results and the effective medium approach. In contrast with the case of the longitudinal constant C_{33} studied through picosecond ultrasonics in the preceding section, we do not observe any significant anomalous softening of C_{44}. From the evaluation of the experimental uncertainties we conclude that the effective medium approach allows calculating C_{44} with a precision of 10%.

IV. CONCLUSIONS

The elastic properties of sputtered deposited single layers and superlattices of permalloy layers with alumina spacers were investigated using both picosecond ultrasonics and Brillouin light scattering techniques. Most of the elastic properties of single polycrystalline permalloy and amorphous alumina have been determined. Very good agreement was found for the longitudinal elastic constant of alumina measured by the two techniques (178 ± 5 GPa versus 176 ± 3 GPa).

Pulse echo measurements in the picosecond ultrasonics experiments gave evidence of a strong softening of the effective longitudinal elastic constant with decreasing multilayer period, reaching 40% in the thinnest bilayers. This elastic anomaly was ascribed to interfacial effects and two models (permalloy volume inhomogeneity and weakly bonded interfaces) are suggested. A relation between the thickness and the softened longitudinal elastic constant of the interfacial region was deduced from these measurements for

the permalloy volume inhomogeneity model. For the weakly bonded interface model, a spring stiffness $\varepsilon^{-1} = 149 \pm 5$ GPa nm^{-1} was obtained. In addition localized surface modes were also observed in some of the multilayers. The existence of such modes and the determination of their frequencies confirmed that perfect interfaces could not be considered in this system. A realistic interval for the interface thickness ($0.34\ \text{nm} \leqslant d_{\text{Int}} \leqslant 0.57\ \text{nm}$) could be deduced and our best fit provided $d_{\text{Int}} = 0.52$ nm and $C_{33}^{(\text{Int})} = 60.5$ GPa. With these values the permalloy volume inhomogeneity model leads to calculated frequencies closer to experimental values than using the model of a weakly bonded interface. It is to be noted that in the present picosecond ultrasonics investigation both propagating waves and localized acoustic modes are exploited. One may also highlight the fact that (for the first time to our knowledge) the effective longitudinal elastic constant of the (Py-Al_2O_3) multilayers studied is analyzed in terms of the reference values obtained experimentally separately for the elastic constants of the individual material components (i.e., Py and Al_2O_3).

In contrast, Brillouin light scattering results show that, in the plane of the film, the softening of the shear elastic constant does not exceed 10% for the lowest period.

As quoted above, magnetization measurements[20] have also been performed on these ultrathin Py layers and the experimental results showed the presence of two distinct magnetization zones in the permalloy layers, giving evidence of the existence of modified interfaces with magnetic properties different from the bulk ones. These observations agree with the results deduced, in this work, from the elastic properties.

Our elastic constants determination should be useful for futher studies of the magnetic anisotropy in this system. In the ultrathin permalloy layers (sandwiched by alumina) a thickness dependent magnetic anisotropy has been found[20,37,49] and analyzed in terms of a stress-induced anisotropy (associated with the inverse magnetostriction[50]). So, for a better insight, stresses have to be determined in these permalloy films and, in most cases, mechanical properties have to be known.

*Present address: Laboratoire de Mécanique Physique, UMR CNRS 5469, Université Bordeaux 1, 351 Cours de la Libération, 33405 Talence Cedex, France.

[1] B. M. Clemens, H. Kung, and S. A. Barnett, MRS Bull. **24**, 20 (1999).
[2] P. Bisanti, M. B. Borodsky, G. P. Felcher, M. Grimsditch, and L. R. Sill, Phys. Rev. B **35**, 7813 (1987).
[3] J. A. Bell, W. R. Bennett, R. Zanoni, G. I. Stegeman, C. M. Falco, and C. T. Seaton, Solid State Commun. **64**, 1339 (1987).
[4] M. R. Khan, C. S. L. Chun, G. P. Felcher, M. Grismditch, A. Kueny, C. M. Falco, and I. K. Schuller, Phys. Rev. B **27**, 7186 (1983).
[5] R. Danner, R. P. Huebener, C. S. L. Chun, M. Grismditch, and I. K. Schuller, Phys. Rev. B **33**, 3696 (1986).
[6] J. A. Bell, W. R. Bennett, R. Zanoni, G. I. Stegeman, C. M. Falco, and F. Nizzoli, Phys. Rev. B **35**, 4127 (1987).
[7] G. Carlotti, D. Fioretto, G. Socino, B. Rodmacq, and V. Pelosin, J. Appl. Phys. **71**, 4897 (1992).
[8] G. Carlotti, G. Gubbiotti, L. Pareti, G. Socino, and G. Turilli, J. Magn. Magn. Mater. **165**, 424 (1997).
[9] B. Perrin, B. Bonello, J. C. Jeannet, and E. Romatet, Physica B **219–220**, 681 (1996).
[10] B. M. Clemens and G. L. Eesley, Phys. Rev. Lett. **61**, 2356 (1988).
[11] E. E. Fullerton, I. Schuller, F. T. Parker, K. A. Svinarich, G. L. Eesley, R. Bhadra, and M. Grimsditch, J. Appl. Phys. **73**, 7370 (1993).
[12] J. A. Jaszczak and D. Wolf, J. Mater. Res. **6**, 1207 (1991).
[13] G. Tas, R. J. Stoner, H. J. Maris, G. W. Rubloff, G. S. Oehrlein, and J. M. Halbout, Appl. Phys. Lett. **61**, 1787 (1992).
[14] C. J. K. Ridcharson, M. J. Ehrlich, and J. W. Wagner, J. Appl. Phys. **85**, 861 (1999).
[15] G. Tas, J. J. Loomis, H. J. Maris, A. A. Bailes III, and L. E. Seiberling, Appl. Phys. Lett. **72**, 2235 (1998).
[16] B. Bonello, F. Armand, J-P. Pradeau, H. Perez, B. Perrin, and G. Louis, J. Appl. Phys. **86**, 4959 (1999).
[17] W. J. Meng, G. L. Eesley, and K. A. Svinarich, Phys. Rev. B **42**, 4881 (1990).
[18] R. Bhadra, M. Grimsditch, J. Murduck, and I. K. Schuller, Appl. Phys. Lett. **54**, 1409 (1989).
[19] O. Lenoble, P. Bauer, J. F. Bobo, H. Fischer, M. F. Ravet, and M. Piecuch, J. Phys.: Condens. Matter **6**, 3337 (1994).
[20] N. Bouterfas, Ph.D. thesis, Université Paris-Sud, 1996.
[21] C. Thomsen, H. T. Grahn, H. J. Maris, and J. Tauc, Phys. Rev. B **34**, 4129 (1986).
[22] H. T. Grahn, H. J. Maris, and J. Tauc, IEEE J. Quantum Electron. **QE-25**, 2562 (1989).
[23] H. T. Grahn, H. J. Maris, J. Tauc, and B. Abeles, Phys. Rev. B **38**, 6066 (1988).
[24] W. Chen, Y. Lu, H. J. Maris, and G. Xiao, Phys. Rev. B **50**, 14 506 (1994).
[25] P. Basséras, S. M. Gracewski, G. W. Wicks, and R. J. D. Miller, J. Appl. Phys. **75**, 2761 (1994).
[26] B. Bonello, B. Perrin, E. Romatet, and J. C. Jeannet, Ultrasonics **35**, 223 (1997).
[27] B. Perrin, C. Rossignol, B. Bonello, and J. C. Jeannet, Physica B **263–264**, 571 (1999).
[28] B. Perrin, B. Bonello, J. C. Jeannet, and E. Romatet, Prog. Nat. Sci. **S6**, 444 (1996).
[29] B. Perrin, in *Systèmes Femtosecondes*, edited by P. Laporte and F. Salin (Saint-Etienne University, Paris, 2001).
[30] C. Rossignol and B. Perrin, Anal. Sci. **17**, s245 (2001).
[31] F. Nizzoli and J. R. Sandercock, in *Dynamical Properties of Solids*, edited by G. K. Horton and A. A. Maradudin (Elsevier Science, New York, 1990).
[32] R. Loudon, Phys. Rev. Lett. **40**, 581 (1978).
[33] V. R. Velasco and F. Garcia Moliner, Solid State Commun. **33**, 1 (1980).
[34] V. Bortolani, A. M. Marvin, F. Nizzoli, and G. Santoro, J. Phys. C **16**, 1757 (1983).

[35] P. Djemia, Ph.D. thesis, Université Paris-Nord, 1998.
[36] G. W. Farnell and E. Adler, in *Physical Acoustics*, edited by W. Mason and R. N. Thurston (Academic, New York, 1972), Vol. IX.
[37] P. Djemia, F. Ganot, and P. Moch, J. Magn. Magn. Mater. **165**, 428 (1997).
[38] B. Perrin and C. Rossignol (unpublished).
[39] D. Lide, *CRC Handbook of Chemistry and Physics* (CRC Press, Boca Raton, 1999).
[40] M. L. Huberman and M. Grimsditch, Phys. Rev. Lett. **62**, 1403 (1989).
[41] X. Zhang, R. S. Bandhu, R. Sooryakumar, and B. T. Jonker, Phys. Rev. B **67**, 075407 (2003).
[42] B. Hillebrands, S. Lee, J. Kim, G. I. Stegeman, H. Cheng, J. E. Potts, and F. Nizzoli, Phys. Rev. Lett. **60**, 832 (1988).
[43] J. R. Dutcher, S. Lee, G. I. Stegeman, and C. M. Falco, Phys. Rev. Lett. **65**, 1231 (1990).
[44] G. Carlotti, G. Socino, and L. Doucet, Appl. Phys. Lett. **66**, 2682 (1995).
[45] P. Djemia, F. Ganot, P. Moch, V. Branger, and P. Goudeau, J. Appl. Phys. **90**, 756 (2001).
[46] N. G. Einspruch and L. T. Claiborne, J. Appl. Phys. **35**, 175 (1964).
[47] M. Grimsditch, Phys. Rev. B **31**, 6818 (1985).
[48] M. J. P. Musgrave, *Crystal Acoustic* (Holden Day, San Francisco, 1970).
[49] H. Hurdequint, J. Magn. Magn. Mater. **242–245**, 521 (2002).
[50] S. Chikazumi and S. H. Charap, *Physics of Magnetism* (Wiley, New York, 1964).